



Predictive model for optimizing the near-field electromagnetic energy transfer in plasmonic nanostructure-involved photocatalysts



Wenhui Feng^a, Bo Wang^a, Zuyang Zheng^a, Zhibin Fang^a, Zhenfeng Wang^a,
Shiying Zhang^b, Yanhua Li^b, Ping Liu^{a,*}

^a Research Institute of Photocatalysis, State Key Laboratory of Photocatalysis on Energy and Environment, Fuzhou University, Fuzhou 350002, PR China

^b Hunan Provincial Collaborative Innovation Center for Environment and Energy Photocatalysis, Changsha University, Changsha 410022, PR China

ARTICLE INFO

Article history:

Received 3 October 2015

Received in revised form

11 December 2015

Accepted 13 December 2015

Available online 17 December 2015

Keywords:

Au/graphene/BiVO₄

Förster resonant energy transfer

Near-field electromagnetic energy transfer

Photocatalysis

SPR

ABSTRACT

Förster resonant energy transfer (FRET) is critical hindrance for improving the solar-energy-conversion efficiency via the near-field electromagnetic energy transfer (NEET) mechanism in the plasmonic nanostructure-involved photocatalysts. Herein, a plasmonic nanoparticle/graphene/semiconductor ternary model system is fabricated successfully. In this fabrication, the thin graphene (RGO) layer covers completely the semiconductor with different facets exposed, and the plasmonic nanoparticles are separated from the semiconductor in a proper distance. This unique architecture raises a new opportunity to optimize surface plasmon resonance (SPR) effect in plasmonic nanostructure-involved photocatalysts by the dual modulation of interfacial layer's thickness and fluorescent frequency, resulting a tremendous improvement in the rates of photocatalytic reactions. Furthermore, this predictive model provides a new idea for the design of high-efficient photocatalysts and may upper limits of SPR-mediated enhancement of photocatalytic performance for plasmonic nanostructure-involved photocatalysts.

© 2015 Elsevier B.V. All rights reserved.

1. Introduction

Recent years have seen that SPR offers a promising scheme for improving solar-energy-conversion efficiency in the field of photocatalysis. That is due to the unprecedented abilities of plasmonic nanostructures to trap light, convert the energy of photons into hot-electron, concentrate electromagnetic fields and scatter electromagnetic radiation [1–4]. Numerous studies have demonstrated that plasmonic-metal/semiconductor composites possess significantly higher rate in various photocatalytic reactions compared with nearby single semiconductors [5–20]. Though the NEET mechanism have been proposed, the deep study to take full advantage of NEET to enhance photocatalytic performance is scarce [4,21–26]. Indeed, rationally strengthening the NEET is an effective but rough approach to further improve photoactivity of the plasmonic metal/semiconductor composite.

As known, photo-excited plasmonic nanostructure is characterized by the existence of strong electric field nearby the metallic nanostructure whose intensity is greatly higher than the field of photons used to photo-excite the nanostructure. This SPR-induced

electromagnetic field is spatially non-homogenous, with the highest intensity at the surface of the nanostructure and decreasing exponentially with distance from the surface within ~20–30 nm. Namely, the near-field electromagnetic mechanism is based on the interaction of the semiconductor with the strong SPR-induced electric field [2]. That energy transfer from a plasmon to the nearby semiconductor through the SPR-induced electric field is plasmon resonance energy transfer (PRET) [1,2]. PRET acts as an antenna to confine the optical energy to the near-surface region of a semiconductor near the plasmonic metal. It means that PRET could effectively change the locations of full-charge carriers in the semiconductor and increase the concentration of photogenerated carriers, which can facilitate the photocatalytic process [1,2,27]. Paradoxically, while a metal surface close the semiconductor to promote PRET, more energy will be quenched via FRET [2,28]. FRET is depicted as energy transfer from the semiconductor (a fluorescent donor, denoted as D) to plasmonic nanostructure (an absorbing acceptor, denoted as A), occurring over similar length scales to those of PRET [29]. Usually, PRET may be considered as a forward reaction for exciting more electron–hole pairs in the semiconductor. FRET, in contrast, can be considered as a back reaction, through which the excited state in the semiconductor quenches without involving charge transfer [30,31]. Generally, FRET and PRET coexist in metal/semiconductor composite, which has been becoming

* Corresponding author. Fax: +86 591 8377 9239.

E-mail address: liuping@fzu.edu.cn (P. Liu).

a tremendous obstacle to exploring the full range of advantages of NEET. Thus, the minimization of the FRET effect and optimization of PRET effect are of great urgency and challenge.

Reportedly, the Förster energy transfer rate (k_{et}) is inverse proportion to the fourth power of the spacing (d^4) for dipole-donor infinite surface-acceptor, and increases exponentially with the Förster radius (R_0) [32]. R_0 can be calculated from the following expression:

$$R_0^6 \sim \frac{9000 \ln 10 \kappa^2 \eta_s^0}{128 \pi^6 n^4 N \nu^4} \int_0^\infty f_s(\nu) \alpha(\nu) d\nu \quad (1)$$

where κ is an orientation factor ($\kappa^2 = 2/3$ for random orientation); η_s^0 is the photoluminescence quantum efficiency of D; n is the refractive index of the embedding medium; N is Avogadro's constant; ν is the wavenumber; f_s is the emission spectrum of D and α is the absorption spectrum of A. Clearly, the less overlap between f_s and α is, the slower k_{et} is. There is also a strong correlation between wavelength and k_{et} . The longer the wavelength is, the higher k_{et} is [1]. Therefore, regulating the fluorescent frequency of D for decreasing the overlap between f_s and α , would be a potential strategy to minimize FRET without reduction of PRET.

In our previous work, we found that the unique model system of thin RGO layer completely coating semiconductor with different facets exposed (RGO/semiconductor) could subdivide the intrinsic fluorescence of semiconductor into two fluorescent emissions with different frequency, via the facet-driven dual-selectivity-channel carrier separation mechanism [33]. It means that this unique structure make it possible to modulate fluorescent frequency of D. Inspired by this fact, we come up with an ideal model for enhancing PRET while limiting the FRET, which is integration of this unique structure with plasmonic nanostructure. Concrete model is listed as follows: Firstly, there must be some overlap between the band-gap absorption of semiconductor and SPR absorption of plasmonic nanostructure to ensure the NEET occurring. Secondly, the interfacial RGO layer should possess an optimal thickness (generally a few nanometers) for compromising the PRET and FRET process [2,4,22]. Thirdly, the selected plasmonic nanostructure could not induce hot-electron so the hot-electron injection effect could be eliminated. Lastly, but most essentially, at least one fluorescent emission does not overlap with the SPR absorption of plasmonic nanostructure, to minimize the overlap between f_s and α . This designed model structure would optimize NEET by lowering the FRET effect.

For the implementation of this concept, we engineer the unique architecture as follows: BiVO_4 with different facets exposed and Au nanospheres (NSs) are respectively chosen as photocatalyst and plasmonic nanostructure due to the overlap between the band gap absorption of BiVO_4 and SPR absorption of Au NSs and the little overlap between one kind of fluorescent emission (~ 440 nm) for RGO/ BiVO_4 and the SPR absorption of Au NSs. In addition, for significant hot electron generation or injection is only found in smaller plasmonic metal nanoparticles (<30 nm) [2,3,34]. Only Au NSs with 50–100 nm in a diameter are utilized in this construction, excluding the enhancements of photoactivity on account of the hot-electron injection. Typically, we synthesize the RGO/ BiVO_4 by our previous method [33]. Then Au NSs (50–100 nm) are deposited on RGO surfaces (to construct Au/RGO/ BiVO_4) by the photo-deposition method.

2. Experimental

2.1. Materials

Bismuth nitrate pentahydrate ($\text{Bi}(\text{NO}_3)_3 \cdot 5\text{H}_2\text{O}$, >99.0%) ammonium vanadate (NH_4VO_3 , >99.9%), ammonia water ($\text{NH}_3 \cdot \text{H}_2\text{O}$, 26–28 wt%), nitric acid (HNO_3 , 26–28 wt%), chloroauric acid

tetrahydrate ($\text{AuCl}_3 \cdot \text{HCl} \cdot \text{H}_2\text{O}$, AR), ethanal absolute ($\text{CH}_3\text{CH}_2\text{OH}$) and methanol absolute (CH_3OH) were purchased from Sinopharm Chemical Reagent Co., Ltd. (Shanghai, China). GO was purchased from Nanjing XFNANO, Inc. All materials were analytical grade and used without any purification process. Deionized (DI) water used in the synthesis came from local sources.

2.2. Synthesis of BiVO_4

BiVO_4 with {1 1 0} and {0 1 0} facets exposed was synthesized by a hydrothermal procedure. Typically, 36 mmol $\text{Bi}(\text{NO}_3)_3 \cdot 5\text{H}_2\text{O}$ and equal amount of NH_4VO_3 were dissolved into 300 mL HNO_3 solution (2 M) and the pH value of the solution was then adjusted to 2.0 with ammonia solution under stirring until formation of an orange precipitate. After about 2 h aging, the orange precipitate at the bottom of the beaker was transferred to a 100 mL Teflon-lined stainless steel autoclave and heated at 200 °C for 24 h and then allowed it cool down. A vivid yellow powder was separated by filtration, washed with DI water for several times. Then the products were dried at 60 °C overnight in vacuum oven.

2.3. Synthesis of GO/ BiVO_4

GO/ BiVO_4 was synthesized through a evaporation-induced self-assembly process. Briefly, 1 g BiVO_4 powders and 20 mg GO were put into 100 mL ethanol and 50 mL DI water respectively, and ultrasound treated for 1 h to disperse the samples evenly. Then the obtained 50 mL GO solution was dropped into the BiVO_4 solution under vigorous stirring and the obtained mixtures were kept stirring for 12 h without sealing in a fuming hood. Then, the residual solution was dried in a 60 °C water bath with stirring. Lastly, the obtained sample was further kept overnight to let the GO combine tightly with BiVO_4 polyhedrons.

2.4. Synthesis of RGO/ BiVO_4

The RGO/ BiVO_4 composites have been fabricated by a mild photoreduction process. In detail, 100 mg GO/ BiVO_4 was dispersed into a breaker containing 80 mL DI water and 20 mL methanol. Then, the solution was irradiated with full-wave band light for 2 h with stirring. Collected the precipitate and washed it with DI water. The final product was dried in a vacuum oven.

2.5. Synthesis of Au/ BiVO_4

The Au/ BiVO_4 composites have been fabricated by a mild photodeposition process. In detail, 100 mg BiVO_4 and a calculated amount of $\text{AuCl}_3 \cdot \text{HCl} \cdot \text{H}_2\text{O}$ (3 wt%) was dispersed into a breaker containing 90 mL DI water and 10 mL methanol, respectively. And the suspension was ultrasounded for 5 min. Then, the solution was irradiated with full-wave band light for 1.5 h under stirring. Collected the precipitate and washed it with DI water. The final product was dried in a vacuum oven.

2.6. Synthesis of Au/RGO/ BiVO_4

The Au/RGO/ BiVO_4 composites have been fabricated by a mild photodeposition process. Normally, 100 mg RGO/ BiVO_4 was dispersed into a breaker containing 90 mL DI water and 10 mL methanol. Subsequently, a calculated amount of $\text{AuCl}_3 \cdot \text{HCl} \cdot \text{H}_2\text{O}$ (3 wt%) was dropwise added into the above suspension under vigorous stirring. Then, the solution was ultrasounded for 5 min and irradiated with full-wave band light under stirring for 1.5 h. Collected the precipitate and washed it with DI water. The final product was dried in a vacuum oven.

2.7. Characterization

The crystal structures of the as-prepared samples were identified by X-ray diffraction using X-ray powder diffraction (XRD) patterns and were carried out on a Bruker D8 ADVANCE X-ray diffractometer, with Cu K α radiation ($\lambda = 0.15418$ nm), which operated at 40 kV and 40 mA. The scan rate was 0.5 (2θ s $^{-1}$). Scanning electron microscopy (SEM) images were obtained using a HITACHI SU8000 field-emission scanning electron microscope. Transmission electron microscopy (TEM) and high-resolution transmission electron micrographs (HRTEM) images were collected with a TecnaiG2F20 S-TWIN with an accelerating voltage of 200 kV. X-ray photoelectron spectroscopy (XPS) investigation was recorded on a Thermo Scientific ESCA Lab 250 system, with a monochromatic Al K α as the X-ray source, hemispherical analyzer, and sample stage with multi-axial adjustability to obtain the composition on the surface of samples. UV–vis diffuse reflectance spectroscopy (DRS) was measured by a Cary 500 UV–vis spectrophotometer, during which BaSO $_4$ was served as the background. The nitrogen adsorption and desorption isotherms were characterized using a Micrometrics ASAP 2020 analyzer at 77 K after the as-prepared samples were degassed at 180 °C for 300 min in a vacuum. The photoluminescence (PL) spectra were obtained using an Edinburgh Analytical Instrument FL/FSTCSPC920 spectrophotometer at an excitation wavelength of 360 nm. Short-circuit transient photocurrent response analysis was conducted using a ZENNIUM electrochemical workstation (Zahner, Germany) with a conventional three-electrode system. The reference and counter electrodes were Ag/AgCl and Pt plate, respectively, and 0.2 M Na $_2$ SO $_4$ (pH 6.8) aqueous solution served as the electrolyte. 10 mg of the as-prepared sample was dispersed in 0.5 mL *N,N*-dimethyl formamide (DMF) solution by sonication, and the slurry (40 μ L) was then evenly spread onto a indium tin oxide (ITO) conductor glass substrate with an area of 5 mm \times 5 mm. Then the glasses covered with samples were dried, and the uncovered parts were painted by insulating epoxy resin. The obtained ITO glass serves as a working electrode. A 300 W Xe lamp was used to provide a visible light source equipped with a cut-off filter ($\lambda > 400$ nm).

2.8. Photocatalytic activity measurement

2.8.1. Photocatalytic degradation of RhB

The photo-degradation of RhB in aqueous solution was done in a Pyrex glass vessel. Typically, 20 mg of the photocatalyst was dispersed into 60 mL of RhB aqueous solution (5 mg L $^{-1}$) in the Pyrex glass vessel. Before light illumination, all suspensions were kept in the dark for 60 min with stirring to ensure the adsorption–desorption equilibrium had been established. Then the suspension was illuminated under a 300 W Xe lamp with a 400 nm cut-off filter, and the photodegradation of RhB was proceed. During the process of photodegradation, the concentrations of RhB in the suspension, collected at interval 20 min, was detected respectively by a Cary-50 UV–vis spectrophotometer. The normalized temporary concentration changes (C/C_0) of RhB solution during the photo-degradation are proportional to the normalized maximum absorbance (A/A_0) and derived from the changes in the dye's absorption profile (554 nm for RhB) at a given time interval.

2.8.2. Photocatalytic degradation of 2-naphthol (2-NAP)

Typically, 20 mg of the photocatalyst was dispersed into 40 mL of 2-NAP aqueous solution (20 μ mol L $^{-1}$) in the Pyrex glass vessel. Before light illumination, all suspensions were kept in the dark for 60 min with stirring to ensure the adsorption–desorption equilibrium had been established. Then the suspension was illuminated under a 300 W Xe lamp with a 400 nm cut-off filter, and the photodegradation of 2-NAP was proceed. During the process of

photodegradation, the concentrations of 2-NAP in the suspension, collected at interval 20 min, was detected respectively by a Cary-50 UV–vis spectrophotometer. The normalized temporary concentration changes (C/C_0) of 2-NAP solution during the photo-degradation are proportional to the normalized maximum absorbance (A/A_0) and derived from the changes in the dye's absorption profile (224 nm for 2-NAP) at a given time interval.

2.8.3. Photocatalytic oxidation of water for O $_2$ production

Typically, 100 mg as-prepared samples were dispersed into 100 mL 0.02 M KIO $_3$ aqueous solution. The suspension was poured into a quartz flask, and vacuumed with a vacuum pump for 2 h to drive away the residual oxygen. The photocatalytic water oxidation was carried out by irradiating the suspension with a 300 W Xe lamp coupled with a cut-off filter ($\lambda > 400$ nm). The temperature of reaction solution was kept at 4 °C. The gas product composition was analyzed every 1 h by an Techcomp 7900 chromatograph (GC) with TCD detector.

3. Results and discussion

X-ray diffraction (XRD) patterns of all BiVO $_4$ -based samples in Fig. 1a show that the diffraction peaks corresponding to the pure monoclinic phase of BiVO $_4$ (*m*-BiVO $_4$) (JCPDS No. 75-1867) arise for all samples. Notably, the appearance of diffraction peaks at 38° and 44° in Fig. 1b, which correspond to the (1 1 1) and (2 0 0) plane of Au nanostructure (JCPDS No. 01-089-3697), respectively, confirms the existence of Au in the Au/BiVO $_4$ and Au/RGO/BiVO $_4$ composites. Besides, no obvious characteristic peaks of RGO are detected in RGO-involved composites probably due to the little RGO. Fig. 2a demonstrates the UV–vis diffuse reflectance spectra (DRS) of as-synthesized samples. In our previous work, the band gap of RGO/BiVO $_4$ was estimated to be 2.33 eV [33], that is, the inter-band absorption of RGO/BiVO $_4$ is cut off at \sim 532 nm. As presented in Fig. 2a, all composites have a much better light absorption ability than bare BiVO $_4$ in the range of 500–800 nm due to the wideband absorption of RGO or the increased scattering of Au NSs. Further extracting the overlap integral for Au/RGO/BiVO $_4$ structure, the UV–vis absorption profile of the Au/RGO/BiVO $_4$ nanostructure is deconvoluted into the RGO/BiVO $_4$ band-gap absorption fitting line and the Au SPR absorption fitting line by a Boltzmann distribution and Gaussian function, respectively, which are displayed in Fig. 2b. Apparently, there is a overlap (ca. 480–530 nm) between band gap absorption of BiVO $_4$ and SPR absorption of Au NSs in the as-obtained Au/RGO/BiVO $_4$ structure. Field-emission scanning electron microscopy (SEM) images of all the as-obtained samples are displayed in Fig. 3, which reveal that all samples have a truncated bipyramid shape. The BiVO $_4$ in RGO/BiVO $_4$ and Au/RGO/BiVO $_4$ (Fig. 3b and d) are covered with thin RGO layer tightly and uniformly, and Au NSs, with the size of 50–100 nm, are dispersed selectively on the two flat and rectangular facets of BiVO $_4$ (Figs. 3 c,d and S1). The crystal structure and orientation of the *m*-BiVO $_4$ octahedron are further investigated by transmission electron micrographs (TEM) and selected area electron diffraction (SAED) observation. As shown in Fig. S2a, BiVO $_4$ possesses uniform decahedral structure, and the corresponding SAED pattern (indexed as [0 1 0] zone) can be indexed as the 2 0 0, 0 0 2 and 2 0 2 reflection. Besides, the angle about 90.4° between (2 0 0) and (0 0 2) in the SAED pattern are consistent with the *m*-BiVO $_4$. Moreover, an angle of \sim 68° is measured between the square facet and isosceles trapezoid plane in Fig. S2b, which is consistent with the theoretical value of the {0 1 0} and {1 1 0} facets of *m*-BiVO $_4$. Clearly, these results indicate that each mono-dispersed octahedron has single-crystal characteristics, and the octahedral BiVO $_4$ crystal is dominantly enclosed by {1 1 0} and {0 1 0} facets. While TEM and

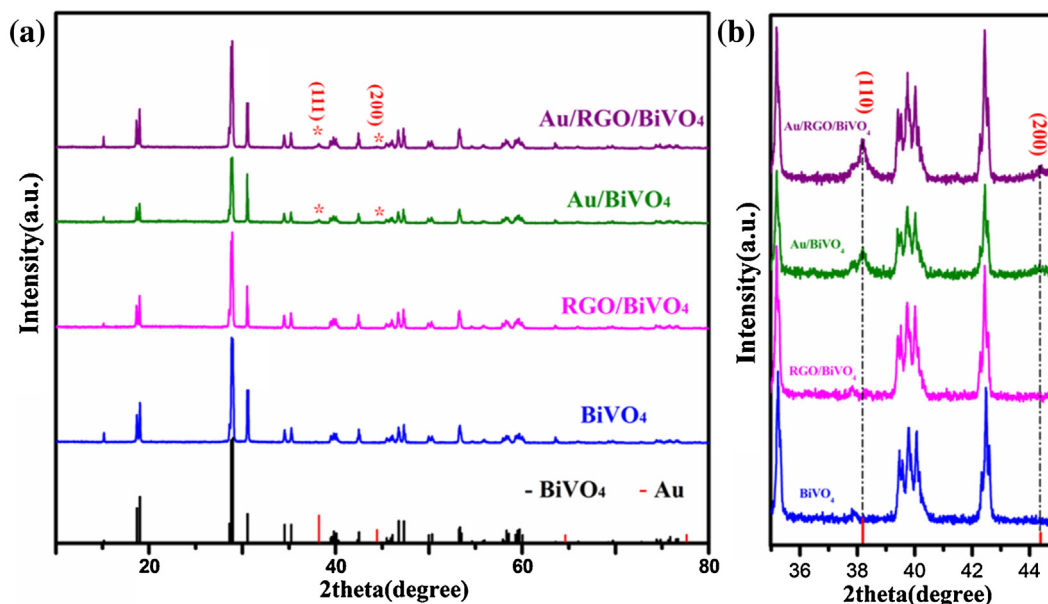


Fig. 1. Typical XRD (a) and HRXRD (b) patterns of all BiVO_4 -based samples.

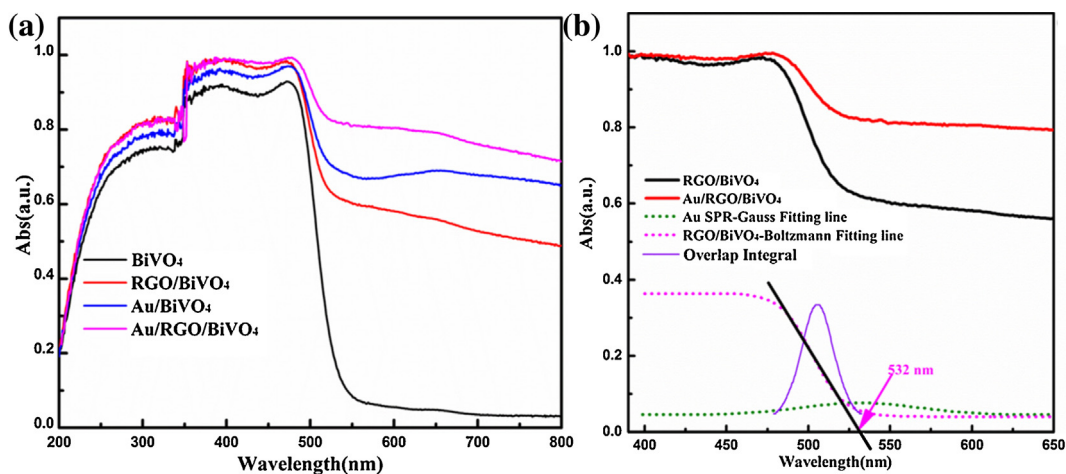


Fig. 2. UV-vis absorption spectra of all BiVO_4 -based samples (a), and the overlap function for Au/RGO/ BiVO_4 composite. The solid black and red line show the experimental UV-vis absorption profile of RGO/ BiVO_4 and Au/RGO/ BiVO_4 . The green dotted curve shows the fit of the SPR with a Gaussian function. The pink dotted line shows the fit of the RGO/ BiVO_4 band gap by Boltzmann distribution. The lavender solid line shows the overlap of RGO/ BiVO_4 band gap and Au SPR (b). (For interpretation of the references to color in this figure legend, the reader is referred to the web version of this article.)

high-resolution transmission electron micrographs (HRTEM) further confirm that 50–100 nm diameter Au NSs are located on the {010} facets of RGO/ BiVO_4 (as shown in Figs. 4 and S1). And the intermediate RGO layer, with the thickness of 2–5 nm, is thin enough to assure that the near field can interact intensively with the semiconductor. In addition, the chemical composition of Au NSs is also verified by X-ray photoelectron spectroscopy (XPS). As shown in Fig. S3, the Au 4f spectrum for Au/ BiVO_4 is identified in two peaks at 84.0 eV and 87.7 eV, which is assigned to metallic Au [35]. However, a negative binding energy shift of around 0.3 eV of two Au 4f peaks is observed for Au/RGO/ BiVO_4 . This significant difference in electronic structures between Au on BiVO_4 and Au on RGO/ BiVO_4 indicates a strong electronic interaction between Au and RGO [36]. This further confirms the tight contact between Au and RGO layer. These results manifest that the expected model is constructed successfully.

The photocatalytic activities of all the samples are evaluated by the photodegradation rate (k) of Rhodamine B (RhB) in the aqueous solution under visible-light irradiation. The corresponding k data is

shown in Fig. 5a. It can be found that the k of RGO/ BiVO_4 exhibits 12 times higher than one of BiVO_4 . The enhanced photoactivity be mainly attributed to the facet-driven dual-selectivity-channel carrier separation mechanism [33]. The k of Au/ BiVO_4 shows about 15 times as high as the k of pristine BiVO_4 . The enhancement of photocatalytic performance may be ascribed to the co-catalyst effect, scattering and near-field electromagnetic mechanisms of Au NSs [37]. Importantly, the Au/RGO/ BiVO_4 shows about 36 times photocatalytic degradation rate of RhB as high as the pristine BiVO_4 , which is higher than the sum of the ones of RGO/ BiVO_4 and Au/ BiVO_4 . As it is possible that the photosensitization of RhB interferes the degradation of RhB. The photocatalytic oxygen production from water and the photodegradation of the colourless 2-NAP under visible-light irradiation are done to prove the desired Au/RGO/ BiVO_4 with unique structure is beneficial to the photocatalysis. As expected, Au/RGO/ BiVO_4 exhibits the best photocatalytic oxygen production rate and degradation rate of 2-NAP among the four samples tested (Figs. 5 b and S4). Moreover, the surface area data of all samples and the kinetic analyses of RhB

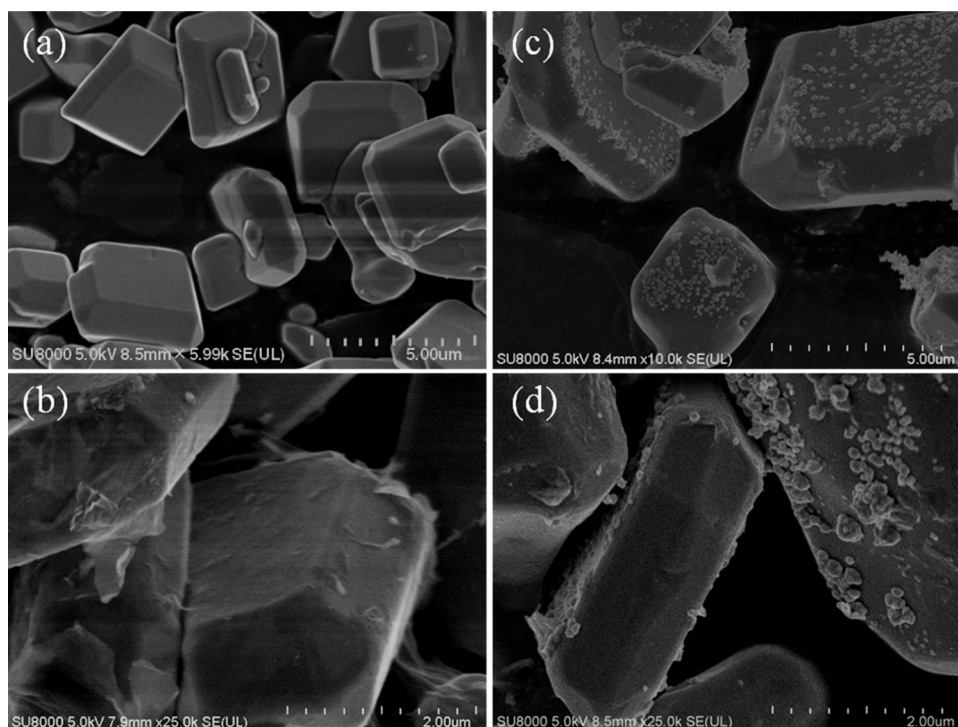


Fig. 3. Typical SEM images of BiVO₄ (a), RGO/BiVO₄ (b), Au/BiVO₄ (c) and Au/RGO/BiVO₄ (d).

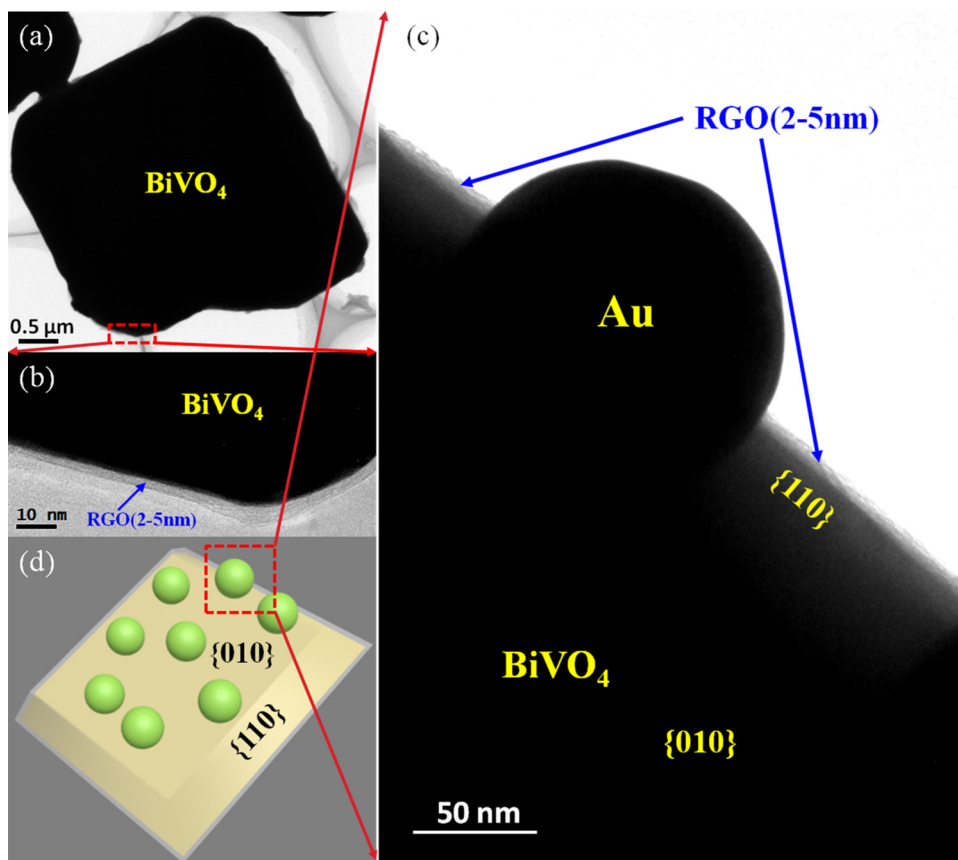


Fig. 4. The TEM images (a), HRTEM images (b and c) and model illustration (d) of Au/RGO/BiVO₄ hybrid.

photodegradation are listed in Table S1. Obviously, Au/RGO/BiVO₄ still exhibits the best normalized kinetic rate for photocatalytic degradation of RhB among the four samples tested. It convincingly

indicates that there exist some kind unique factor, resulting the superior photocatalytic performance for Au/RGO/BiVO₄, except for the influence of surface area. In addition, the photocatalytic perfor-

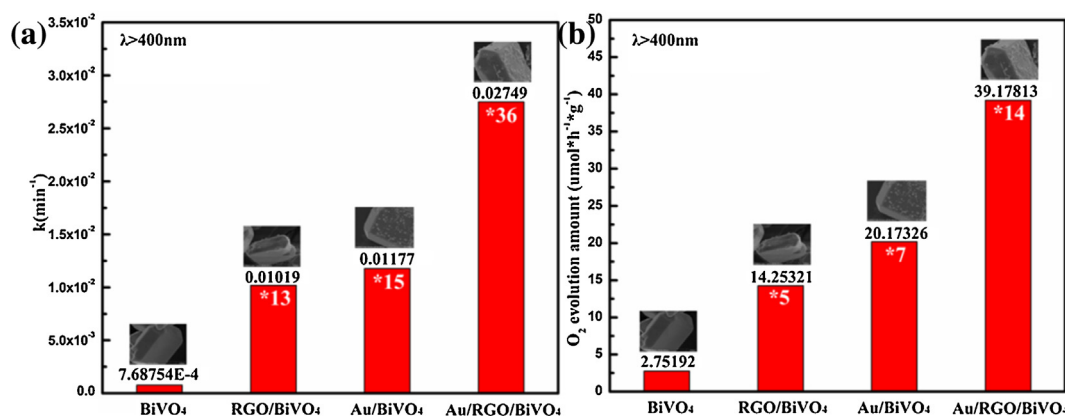


Fig. 5. The linear fitting pseudo-first-order reaction rate (k) of photodegradation of RhB (a) and photocatalytic water oxidation performance (b) over all samples under visible light irradiation.

mance only shows a slight decrease after the photodegradation is operated consecutively three times as displayed in Fig. S5. It might indicate that the obtained Au/RGO/BiVO_4 also has good stability.

In order to reveal the factors for the superior photocatalytic performance in Au/RGO/BiVO_4 , room-temperature photoluminescence (PL) measurement is operated. Fig. 6a presents the PL emission spectra of BiVO_4 , RGO , RGO/BiVO_4 , Au/BiVO_4 and Au/RGO/BiVO_4 . As displayed, for RGO/BiVO_4 and Au/RGO/BiVO_4 composites, two broad bands centered around at 560 nm and 440 nm are detected. Former is corresponding to the recombination of the band-gap photo-excited electron-hole pairs, and the latter is the recombination of photoexcited electrons on {110} facets and the photogenerated holes on {010} facets through the RGO layer [33]. For Au/BiVO_4 hybrid, the broad PL peak at ca. 560 nm slightly weaker than that of BiVO_4 . This phenomenon mainly results from the fact that Au NSs act as a electron sinker, inhibiting the recombination of photo-induced electron-hole pairs in BiVO_4 [37]. Besides, it is reported that the radiative recombination process of self-trapped excitation could be inhibited effectively via the shunt-channel for carrier separation in RGO/BiVO_4 composite [33]. So the intensity of PL band at ca. 560 nm for RGO/BiVO_4 also decreased obviously. Surprisingly, when Au NSs are introduced onto RGO/BiVO_4 hybrid (Au/RGO/BiVO_4), the intensity of the two bands rise to the highest among all samples concurrently, with non-geometrical enhancement. It is clear that the enhancement of the peak at 440 nm is considerably larger than that of the band at 560 nm. This non-geometrical enhancement for the two PL broad bands probably derives from the following facts. Firstly, the SPR of the Au NSs is excited by the intrinsic fluorescence of BiVO_4 . Subsequently, the plasmonic Au nanostructures concentrate extremely the intrinsic fluorescence and induce concentrated electromagnetic fields around the metallic nanostructure. This SPR-induced near-field interacts with nearby BiVO_4 , and excites more free carriers. Therefore, more recombination of photoinduced hole-electron pairs are exhibited. In addition, Au/RGO/BiVO_4 shows the higher intensity of PL emission at ~ 560 nm compared with Au/BiVO_4 , which indicates higher NEET efficiency. Here are the possible reasons: on one hand, the 2–5 nm interface RGO layer could separate BiVO_4 and plasmonic Au NSs. It is reported that this spacing can optimize the NEET by compromising the PRET and FRET effect [2,4,22]. On the other hand, it is attributable to the lower FRET effect, resulting from the no overlap between SPR absorption of plasmonic Au NSs and the fluorescent emission with shorter wavelength (~ 440 nm). Thus, the interface RGO layer in our designed system enhances the NEET efficiency via its thickness and change of fluorescent frequency. Furthermore, the distinction between above-mentioned two contributors and a deeper analysis of their

interrelationship in photocatalytic process are ongoing. Meanwhile, the transient photocurrent response, displayed in Fig. 6b, is proportional to the photoactivity for all samples. This is further evidence that Au/RGO/BiVO_4 generates the most free carriers among four samples. To confirm whether the Au SPR is responsible for the increased photogenerated carriers which result in the dramatic enhancement of photoactivity, the transient photocurrent responses of bare BiVO_4 and Au/RGO/BiVO_4 under different incident light irradiation with different wavelength are detected, respectively. Transmission spectra of light source with different pass filter are presented in Fig. S6. Fig. 6c shows the photocurrent of BiVO_4 and Au/RGO/BiVO_4 irradiated with $\lambda = 410 \pm 20$ nm, $\lambda = 505 \pm 30$ nm and $\lambda = 600 \pm 20$ nm light. Distinctly, the photocurrent of Au/RGO/BiVO_4 shows an increase compared with BiVO_4 under different light irradiation. But the enhancement ratios are significantly different (Fig. 6d). A significant enhancement in photocurrent ($20.6\times$) under $\lambda = 505 \pm 30$ nm light irradiation, which light could excite BiVO_4 and Au SPR simultaneously (that is necessary for the occurrence of NEET in plasmonic nanostructure-involved photocatalysts), and the enhancement ratios are 4.0 and 3.2 under $\lambda = 410 \pm 20$ nm and $\lambda = 600 \pm 20$ nm light irradiation, which light excites either BiVO_4 or Au SPR, those provide favorable evidence for that plasmonic Au NPs dominantly contributing to the enhanced photocurrent under visible light irradiation and resulting superior photocatalytic performance via optimal NEET mechanism in Au/RGO/BiVO_4 .

Based on the above experimental results and theoretical analysis, a possible mechanism for explaining the superior photocatalytic property of Au/RGO/BiVO_4 composite is illustrated in Scheme 1. When Au/RGO/BiVO_4 is exposed in the visible-light irradiation, the VB electrons of BiVO_4 are photoexcited to the CB, creating holes in the VB. While the Au SPR is also photoexcited, inducing strong electromagnetic field around, the plasmonic Au interacts with the nearby BiVO_4 and more free charge carriers are generated. The more photogenerated electron-hole pairs results the more carrier recombination, showing more intense PL emission, which would accelerate FRET rate. However, previous study have demonstrated that the photogenerated carriers in RGO/BiVO_4 would separated via the facet-driven charge dual-selectivity-channel separation mechanism. More importantly, the unique charge separation can effectively inhibit the band-gap PL emission around 560 nm, which overlaps significantly with the SPR absorption of plasmonic Au nanospheres, and induce a new kind of fluorescent emission with higher frequency. Even, the new emission overlaps little with the SPR absorption of plasmonic Au, lowering relatively the FRET effect. Besides, interfacial RGO layer, with proper thickness, also optimizes the NEET by compromising the PRET and FRET effect. Overall,

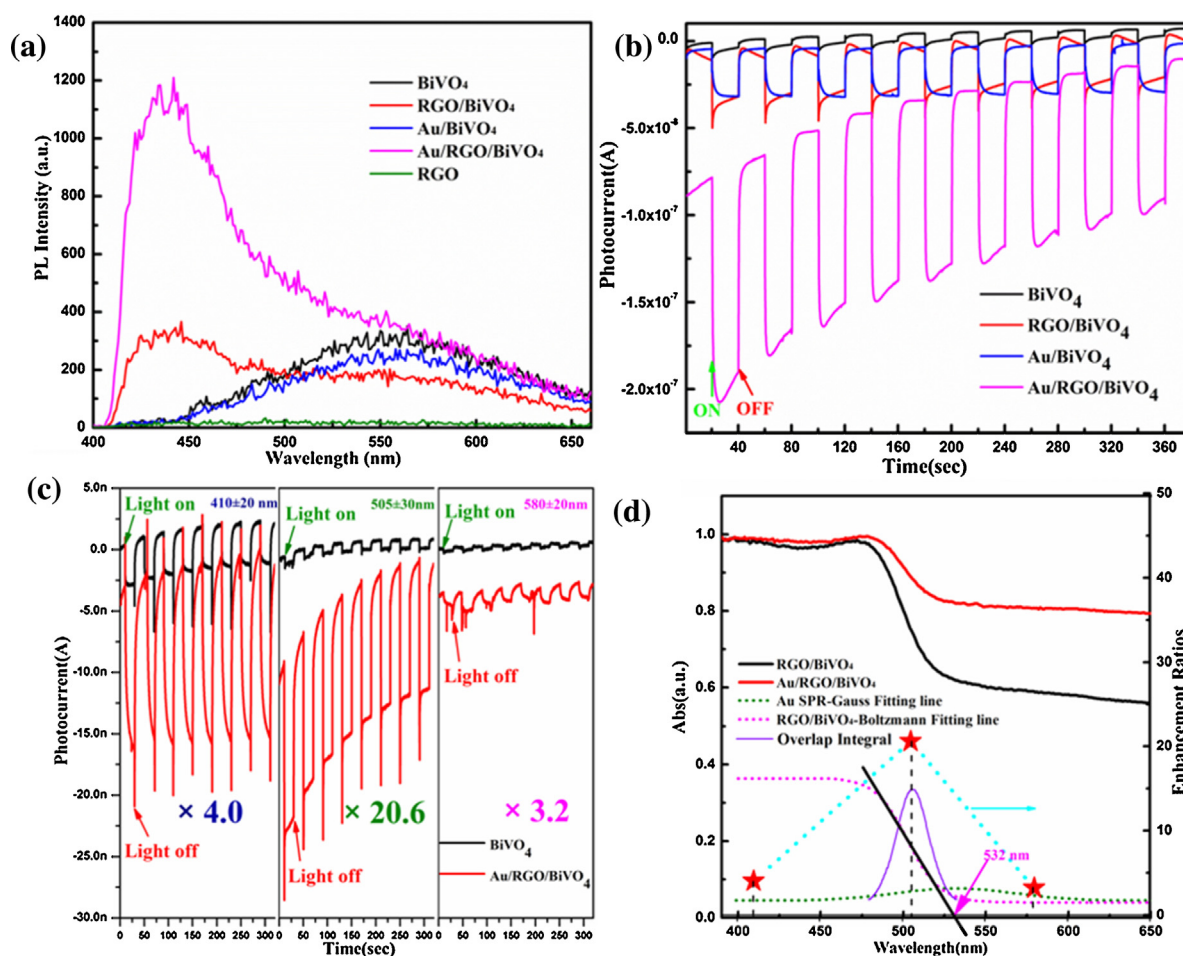
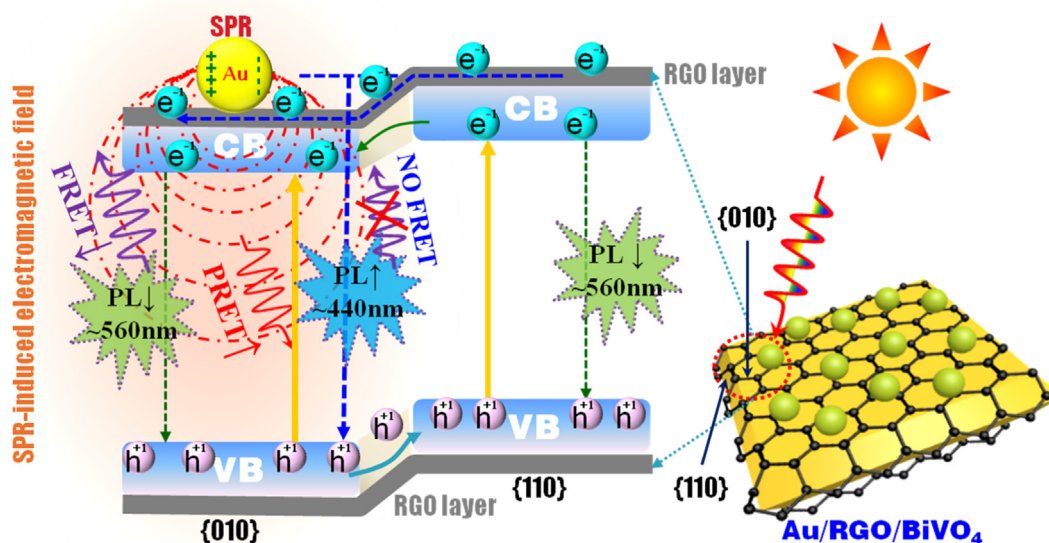


Fig. 6. (a) PL spectra of all samples. (b) Short-circuit transient photocurrent response of BiVO₄-involved composites under visible light irradiation ($\lambda > 400$ nm). (c) The photocurrent of BiVO₄ and Au/RGO/BiVO₄ irradiated with $\lambda = 410 \pm 20$ nm, $\lambda = 505 \pm 30$ nm and $\lambda = 600 \pm 20$ nm light. (d) The experimental UV-vis spectra, the Au SPR-Gauss fitting absorption line, the RGO/BiVO₄-Boltzmann fitting absorption line, and the photocurrent enhancement ratios of Au/RGO/BiVO₄ compared to BiVO₄ under different light irradiation.

in our designed plasmonic metal-involved architecture, the RGO interfacial layer controls the separation distance between plasmonic metal and semiconductor, optimizes the NEET efficiency.

As well as the further optimization of NEET is achieved by changing carriers recombination route and adjusting the fluorescent emission frequency based on the unique facet-driven charge dual-



Scheme 1. Schematic representation of the near-field electromagnetic energy transfer mechanism occurs in Au/RGO/BiVO₄.

selectivity-channel separation. Consequently, the photocatalytic performance of plasmonic metal-involved photocatalysts improves dramatically.

4. Conclusions

In summary, we put forward a unique model architecture in which plasmonic nanostructures deposited on the system of semiconductor with different facets exposed wrapped completely by thin RGO layer. In the designed fabrication, not only interfacial RGO layer separates the plasmonic nanostructures and semiconductor in a optimal distance to strengthen the NEET by compromising the PRET and FRET effect, but also RGO/semiconductor system can guide the route of carrier recombination, decrease the extent of overlap between the emission of D and the absorption of A by regulating the fluorescent frequency to further weaken the FRET effect. As a result, the Au/RGO/BiVO₄ with the predicted structure exhibits remarkable improvement of photocatalytic performance. Two key factors, the thickness of isolation layer and fluorescent frequency of D, are synergistically regulated to optimize the NEET for dramatic enhancement of photoactivity. Moreover, this design concept may broaden our vision to construct high-efficiency plasmonic nanostructure-involved photocatalysts, which may show a good prospect.

Acknowledgements

The authors acknowledge the support from National Natural Science Foundation of China (21473031, 21173046 and 21273035), the funding under National Basic Research Program of China (973 Program: 2013CB632405), National Key Technologies R & D Program of China (2014BAC13B03) and Science & Technology Plan Project of Fujian Province (2014Y2003).

Appendix A. Supplementary data

Supplementary data associated with this article can be found, in the online version, at <http://dx.doi.org/10.1016/j.apcatb.2015.12.027>.

References

- [1] S.C. Warren, E. Thimsen, *Energy Environ. Sci.* 5 (2012) 5133–5146.
- [2] S. Linic, P. Christopher, D.B. Ingram, *Nat. Mater.* 10 (2011) 911–921.
- [3] C. Clavero, *Nat. Photonics* 8 (2014) 95–103.
- [4] S.K. Cushing, J. Li, F. Meng, T.R. Senty, S. Suri, M. Zhi, M. Li, A.D. Bristow, N. Wu, *J. Am. Chem. Soc.* 134 (2012) 15033–15041.

- [5] Y. Tian, T. Tatsuma, *J. Am. Chem. Soc.* 127 (2005) 7632–7637.
- [6] A. Primo, A. Corma, H. Garcia, *Phys. Chem. Chem. Phys.* 13 (2011) 886–910.
- [7] E. Kowalska, R. Abe, B. Ohtani, *Chem. Commun.* (2009) 241–243.
- [8] A. Furube, L. Du, K. Hara, R. Katoh, M. Tachiya, *J. Am. Chem. Soc.* 129 (2007) 14852–14853.
- [9] K. Awazu, M. Fujimaki, C. Rockstuhl, J. Tominaga, H. Murakami, Y. Ohki, N. Yoshida, T. Watanabe, *J. Am. Chem. Soc.* 130 (2008) 1676–1680.
- [10] A. Primo, T. Marino, A. Corma, R. Molinari, H. Garcia, *J. Am. Chem. Soc.* 133 (2011) 6930–6933.
- [11] Y. Nishijima, K. Ueno, Y. Kotake, K. Murakoshi, H. Inoue, H. Misawa, *J. Phys. Chem. Lett.* 3 (2012) 1248–1252.
- [12] S. Mubeen, J. Lee, N. Singh, S. Kramer, G.D. Stucky, M. Moskovits, *Nat. Nanotechnol.* 8 (2013) 247–251.
- [13] M.W. Knight, Y. Wang, A.S. Urban, A. Sobhani, B.Y. Zheng, P. Nordlander, N.J. Halas, *Nano Lett.* 13 (2013) 1687–1692.
- [14] D.B. Ingram, S. Linic, *J. Am. Chem. Soc.* 133 (2011) 5202–5205.
- [15] S.K. Cushing, J. Li, J. Bright, B.T. Yost, P. Zheng, A.D. Bristow, N. Wu, *J. Phys. Chem. C* 119 (2015) 16239–16244.
- [16] J. Long, H. Chang, Q. Gu, J. Xu, L. Fan, S. Wang, Y. Zhou, W. Wei, L. Huang, X. Wang, P. Liu, W. Huang, *Energy Environ. Sci.* 7 (2014) 973.
- [17] H. Li, Z. Bian, J. Zhu, Y. Huo, H. Li, Y. Lu, *J. Am. Chem. Soc.* 129 (2007) 4538–4539.
- [18] Z. Bian, J. Zhu, F. Cao, Y. Lu, H. Li, *Chem. Commun.* (2009) 3789–3791.
- [19] D. Zhang, M. Wen, S. Zhang, P. Liu, W. Zhu, G. Li, H. Li, *Appl. Catal. B: Environ.* 147 (2014) 610–616.
- [20] W. Zhu, P. Liu, S. Xiao, W. Wang, D. Zhang, H. Li, *Appl. Catal. B: Environ.* 172–173 (2015) 46–51.
- [21] D.B. Ingram, P. Christopher, J.L. Bauer, S. Linic, *ACS Catal.* 1 (2011) 1441–1447.
- [22] M.K. Kumar, S. Krishnamoorthy, L.K. Tan, S.Y. Chiam, S. Tripathy, H. Gao, *ACS Catal.* 1 (2011) 300–308.
- [23] Z. Liu, W. Hou, P. Pavaskar, M. Aykol, S.B. Cronin, *Nano Lett.* 11 (2011) 1111–1116.
- [24] M.A. Mahmoud, W. Qian, M.A. El-Sayed, *Nano Lett.* 11 (2011) 3285–3289.
- [25] C. Yu, G. Li, S. Kumar, H. Kawasaki, R. Jin, *J. Phys. Chem. Lett.* 4 (2013) 2847–2852.
- [26] T.-H. Yang, Y.-W. Harn, M.-Y. Pan, L.-D. Huang, M.-C. Chen, B.-Y. Li, P.-H. Liu, P.-Y. Chen, C.-C. Lin, P.-K. Wei, L.-J. Chen, J.-M. Wu, *Appl. Catal. B: Environ.* 181 (2016) 612–624.
- [27] J. Lee, T. Javed, T. Skeini, A.O. Govorov, G.W. Bryant, N.A. Kotov, *Angew. Chem. Int. Ed.* 45 (2006) 4819–4823.
- [28] A.O. Govorov, G.W. Bryant, W. Zhang, T. Skeini, J. Lee, N.A. Kotov, J.M. Slocik, R.R. Naik, *Nano Lett.* 6 (2006) 984–994.
- [29] T. Förster, *Discuss. Faraday Soc.* 27 (1959) 7.
- [30] A.O. Govorov, J. Lee, N.A. Kotov, *Phys. Rev. B* 76 (2007).
- [31] P.L. Hernández-Martínez, A.O. Govorov, *Phys. Rev. B* 78 (2008).
- [32] J.I. Basham, G.K. Mor, C.A. Grimes, *ACS Nano* 4 (2010) 1253–1258.
- [33] W. Feng, S. Weng, Z. Zheng, Z. Fang, P. Liu, *Chem. Commun.* 51 (2015) 11186–11189.
- [34] C. Burda, X. Chen, R. Narayanan, M.A. El-Sayed, *Chem. Rev.* 105 (2005) 1025–1102.
- [35] T.F. Jaramillo, S.H. Baeck, B.R. Cuenya, E.W. McFarland, *J. Am. Chem. Soc.* 125 (2003) 7148–7149.
- [36] T.-T. Yang, W.-T. Chen, Y.-J. Hsu, K.-H. Wei, T.-Y. Lin, T.-W. Lin, *J. Phys. Chem. C* 114 (2010) 11414–11420.
- [37] S.W. Cao, Z. Yin, J. Barber, F.Y. Boey, S.C. Loo, C. Xue, *ACS Appl. Mater. Interfaces* 4 (2012) 418–423.